First-principles study of *L*-shell iron and chromium opacity at stellar interior temperatures

Valentin V. Karasiev [1,*] S. X. Hu [1] Nathaniel R. Shaffer [1] and Gennady Miloshevsky [2]
[1]*Laboratory for Laser Energetics, University of Rochester, 250 East River Road, Rochester, New York 14623, USA*
[2]*Department of Mechanical and Nuclear Engineering, Virginia Commonwealth University, Richmond, Virginia 23284, USA*

(Received 6 September 2022; accepted 23 November 2022; published 19 December 2022)

Recently developed free-energy density functional theory (DFT)-based methodology for optical property calculations of warm dense matter has been applied for studying *L*-shell opacity of iron and chromium at $T = 182$ eV. We use Mermin–Kohn–Sham density functional theory with a ground-state and a fully-temperature-dependent generalized gradient approximation exchange-correlation (XC) functionals. It is demonstrated that the role of XC at such a high-T is negligible due to the total free energy of interacting systems being dominated by the noninteracting free-energy term, in agreement with estimations for the homogeneous electron gas. Our DFT predictions are compared with the radiative emissivity and opacity of the dense plasma model, with the real-space Green's function method, and with experimental measurements. Good agreement is found between all three theoretical methods, and in the bound-continuum region for Cr when compared with the experiment, while the discrepancy between direct DFT calculations and the experiment for Fe remains essentially the same as for plasma-physics models.

DOI: 10.1103/PhysRevE.106.065202

I. INTRODUCTION

Accurate prediction of optical properties of matter across a wide range of material densities and temperatures is of great importance in planetary science, astrophysics, and inertial confinement fusion (ICF) [1–4]. For example, uncertainties in calculations of solar interior opacities can potentially affect predictive capabilities of solar models. Building a reliable opacity model for materials under extreme condition is one of the grand challenges in high-energy-density physics (HEDP), especially across the most complicated warm-dense-matter (WDM) domain of thermodynamic conditions when both the Coulomb coupling parameter and the electron degeneracy are close to unity. The traditional opacity models based on physics of isolated atoms when the important plasma density and temperature effects such as Stark broadening, ionization potential depression (IPD), and continuum lowering are incorporated via corrections [5–13], often become unreliable beyond the ideal plasma conditions [14–19].

A *first-principles* approach based on finite-temperature density functional theory (DFT) [20] treats deeply bounded core and free electrons on an equal footing, provides a fully self-consistent calculation of screening effects, and as a consequence, allows a fully consistent calculation of the IPD and continuum-lowering effects. Quasistatic pressure broadening due to interaction with neighboring ions and respective shift of energy levels on individual ions is taken into account in DFT-based *ab initio* molecular dynamics (AIMD) simulations. Such simulations become prohibitively expensive, however, in the case of low material density (i.e., a large real-space size simulation cell) and explicit treatment of all electrons with bare Coulomb or an all-electron pseudopotential and huge number of thermally occupied bands required for optical calculations using the Kubo–Greenwood (KG) formalism [21,22] at a wide range of x-ray photon energies. A method recently proposed in Ref. [23] drastically alleviates these computational challenges. The method combines the usual supercell molecular dynamics (MD) simulations with a *single-atom-in-a-cell* calculation at the same thermodynamic conditions with the same periodic boundary condition. The supercell MD results take into account effects due to interactions with neighboring ions required to describe x-ray absorption near-edge structure (XANES) and extended x-ray absorption fine structure (EXAFS). Since short-wavelength interactions mainly probe the local plasma environment, single-atom-in-a-cell calculations can give reasonably good results for high-energy photon absorptions in *L*- and *K*-edge tail regions.

In this work we use this *first-principles* methodology to calculate optical properties (mass-absorption coefficient and opacity) of Cr and Fe at stellar interior temperatures corresponding to recent experiments [14,19]. The purpose is to explore whether such *ab initio* calculations can resolve the reported disagreement between previous atomic physics calculations and measured data [14,19]. The methods used in previous calculations in particular include an average atom model based on time-dependent DFT [24], and calculation of opacity from two-photon processes [25,26]. Our DFT results are compared with the real-space Green's function (RSGF) method [27–29] and to the radiative emissivity and opacity of dense plasmas (REODP) atomistic model [30]. We found good agreement on Cr and Fe among all three theoretical predictions in the bound-continuum region corresponding to the *L* edge tail, and agreement in the same region on Cr when compared with the experiment. However, the

*vkarasev@lle.rochester.edu

difference between direct DFT calculations and the experiment for Fe remains essentially the same as for other plasma-physics models.

The paper is organized as follows: The next section introduces details of the DFT-based methodology including a simple way of computing the average ionization state from DFT data (Sec. II A). In Sec. II B we present orbital-free DFT simulations. Computational details and some convergence tests are presented in Sec. II C. Section III describes our main results for the opacity of low-density iron and chromium at stellar interior temperatures, and Sec. IV provides a short summary of this work.

II. METHOD

A free-energy DFT-based methodology for optical property calculations in the WDM domain presented in Ref. [23] handles deeply bounded core electrons in an equal footing with free electrons in the system and takes into account in a self-consistent way effects such as quasistatic pressure broadening due to interaction with neighboring ions (in case of calculations on MD multi-ion supercell snapshots), the IPD, continuum lowering, and Fermi-surface rising. The methodology incorporates a combination of the KG optical data, evaluated on a set of the AIMD snapshots, with a periodic *single-atom-in-a-cell* calculation at the same thermodynamic conditions. KG calculations on snapshots account for the influence of the local plasma environment, which is important for photon energies near the L and K edges. Kubo–Greenwood data from periodic calculations with single atom cover the tail regions beyond the L and K edges, closing the photon energy gap between the L and K edges and extending the K edge tail toward many-keV photon energies. This gap and short extension beyond the K edge arise in the standard scheme due to a prohibitively large number of bands required for the Kubo–Greenwood calculations with AIMD snapshots.

The Kubo–Greenwood formulation implemented in post-processing code named KGEC (Kubo Greenwood Electronic Conductivity) for use with QUANTUM-ESPRESSO large-scale DFT-based simulation package, KGEC@QUANTUM-ESPRESSO [31,32], calculates the frequency-dependent real and imaginary parts of electric conductivity, $\sigma_1(\omega)$ and $\sigma_2(\omega)$, the real part of the index of refraction, $n(\omega)$, the absorption coefficient, $\alpha(\omega) = \sigma_1(\omega)\frac{4\pi}{n(\omega)c}$, and the mass absorption coefficient $\alpha_{\mathrm{m}}(\omega) = \alpha(\omega)/\rho$ (where c is the speed of light, ρ is the material density, and the photon energy is $\hbar\omega = h\nu$). See Appendix for further details. The optical properties were calculated for a single-atom-in-a-cell and as an average over a selected set of uncorrelated two-atom MD snapshots. Eventually the grouped Rosseland mean opacities for a narrow group of photon energies between $\hbar\omega_1$ and $\hbar\omega_2 = \hbar\omega_1 + \hbar\Delta\omega$ (with $\hbar\Delta\omega = 4$ eV) in the range between 0 and 3 keV are calculated as follows:

$$\kappa_{\mathrm{R}}(\omega_1 : \omega_2) = \frac{\int_{\omega_1}^{\omega_2} n^2(\omega)\frac{\partial B(\omega,T)}{\partial T}d\omega}{\int_{\omega_1}^{\omega_2} n^2(\omega)\alpha_{\mathrm{m}}^{-1}(\omega)\frac{\partial B(\omega,T)}{\partial T}d\omega}, \qquad (1)$$

where the Planck blackbody radiation energy density distribution $B(\omega, T) = (\hbar\omega^3/4\pi^3c^2)/(e^{\hbar\omega/k_{\mathrm{B}}T} - 1)$ depends on the photon frequency and the plasma temperature. The Rosseland mean opacity, Eq. (1), uses a temperature derivative of the Planck function, $\partial B(\omega, T)/\partial T$, as the weighting function and represents one of the commonly used ways to define the average opacity [33,34].

Accuracy of the methodology was confirmed by comparison to NIST reference data for silicon at near-ambient conditions [23]. Recently, a good agreement was found between the DFT predictions and RSGF method for Si at selected warm, dense thermodynamic conditions [29].

Our DFT predictions for the chromium and iron opacity are compared with two recently developed methods: The radiative emissivity and opacity of dense plasmas model and the real-space Green's function method. The REODP model [30] is comprised of two linked submodels: (1) the post Hartree-Fock-Slater (HFS) and Hartree-Fock (HF) models accounting for the near-degenerate states (multiconfiguration method) and correlations of electronic motions with respect to each other (configuration-interaction method), and (2) Collisional-Radiative Steady-State (CRSS) model. The inclusion of static and dynamic electron correlations allows us to go beyond the mean-field approximation of the electron interactions used in HFS and HF as well as DFT methods [35].

In the REODP code there are two implementations of the effects of dense plasma environment. In the first approach the atomic data (wave functions, energy levels, etc.) are calculated for the isolated (free) atoms and then the plasma density effects such as the ionization potential depression using the Stewart and Pyatt model [36,37], continuum lowering, and shift in positions of spectral lines and their broadening are taken into account within the CRSS model [30]. This approach is used in the present calculations of Fe and Cr opacities. In the second approach, the HFS-HF quantum models initially developed for isolated atoms are modified using the ion-sphere approximation to include the effects of a dense plasma on wave functions and energy levels of atoms and ions. A hard wall potential is added to the Hamiltonian in order to force the wave functions to zero on the outer boundary of atom for radial distances greater than the radius of ion sphere [35]. With the decrease of a sphere radius corresponding to the increase of plasma density, the outer-shell wave functions are perturbed, the energies of outermost atomic levels increase, and the electrons become unbounded within a spherical volume. The distorted HFS-HF wave functions and modified orbital energies are used to calculate the atomic data such as transition probabilities, ionization potentials, oscillator strengths, broadening constants, photoionization cross sections, etc. These atomic data are then used in the CRSS plasma model. This second approach, however is not well stable when the treatment of multiply ionized ions is required.

The nonlocal thermodynamic equilibrium CRSS model solves the system of kinetic rate equations for collisional and radiative processes in a plasma in order to determine populations of atomic levels in ions that are used for calculating the number density of different ionic species and free electrons. The concentrations of different type of ions and free electrons are used to calculate the thermodynamic and optical properties of high energy density plasmas. Thus, in either of two ways the REODP model accounts for the effects of dense plasma environment on the wave functions and energy levels of ions that affect the continuum lowering, pressure ionization, shifts

of spectral lines, broadening of lines and change of their shapes.

The RSGF method described in Ref. [29] uses a multicenter expansion to solve the electronic structure problem. Each atom is assigned to a polyhedral zone in which the DFT potential is treated in a muffin-tin approximation, similar to an average atom (AA) model [38]. Corrections to the electronic structure due to scattering between zones is negligible for hot dense plasmas, making RSGF useful for efficient DFT-based opacity calculations. Being a multicenter approach, the continuum lowering and ionization potential depression are naturally included. Some broadening is also accounted for, due to variations in the electronic structure from atom to atom. In this way, the RSGF method may be viewed as introducing multicenter corrections to AA opacities based on a single center [39].

A. Ionization state from density functional theory simulations

The *L*-shell iron opacity measured at Sandia National Laboratories [14] corresponds to the inferred temperature and free-electron density values of $T = 2.11$ MK (≈182 eV) and $n_e = 3.1 \times 10^{22}$ cm^{-3}. Later measurements on chromium and nickel were performed at similar conditions [19]. The density of free electrons in a system is determined by the average ionization state. The Mermin–Kohn–Sham (MKS) DFT calculates the one-electron states and corresponding Fermi–Dirac (FD) occupations, thereby making it possible to predict the number of free electrons in the continuum and free-electron density for each thermodynamic condition. At finite T, the density of states (DOS) consists of a nearly discrete part corresponding to bound electrons followed by a densely distributed quasicontinuous part corresponding to free-electron (continuum) states. The energy of the continuum edge, E_c, can be readily identified from calculated DOS data: Bound levels merge the continuum at E_c when DOS as a function of energy, $g(E)$, changes behavior to the typical homogeneous electron gas (HEG) result

$$g(E) \propto \sqrt{E - E_c}. \tag{2}$$

The number of free electrons in the simulation box can be found by integrating the DOS multiplied by Fermi–Dirac occupations

$$N_{\text{free}} = \int_{E_c}^{\infty} g(E) f_{\text{FD}}(E) dE, \tag{3}$$

where

$$f_{\text{FD}}(E) = \frac{1}{e^{\beta(E-E_F)} + 1}, \tag{4}$$

with $\beta = 1/k_B T$, and E_F is the Fermi-level energy. The free-electron density is calculated by dividing the number of free electrons by the simulation cell volume, $n_{\text{free}} = N_{\text{free}}/\Omega$, and the average ionization state is equal to $Z = N_{\text{free}}/N_{\text{ions}}$, where N_{ions} is the total number of ions in a simulation.

Application of the approach to calculating the ionization state of cold rarefied hydrocarbon (CH) plasmas was reported in Ref. [40]. These calculations were cross-validated by comparisons between DFT-based results and the Saha–Fermi–Debye–Hückel (SFDH) ones based on the free-energy minimization approach (see details in Ref. [40]). After this cross-validation, we use the method to calculate the free-electron density reported in experimental measurements on Fe and Cr ($n_{\text{free}} = 3 \times 10^{22}$ cm^{-3} at $T = 182$ eV) to infer corresponding material density conditions. We performed single-atom-in-a-cell calculations for Fe and Cr at $T = 182$ eV with the corresponding material densities, calculated the average ionization state and free-electron density. These results gave material densities of $\rho_{\text{Fe}} = 0.165$ g/cm^3 and $\rho_{\text{Cr}} = 0.161$ g/cm^3 corresponding to the free-electron density reported in experiments. Figure 1 illustrates the calculation of the average ionization state. DOS behavior changes to the HEG form in Eq. (2) at $E_c \approx 0$. We also emphasize that the integrated occupation (solid red line in Fig. 1) defined as

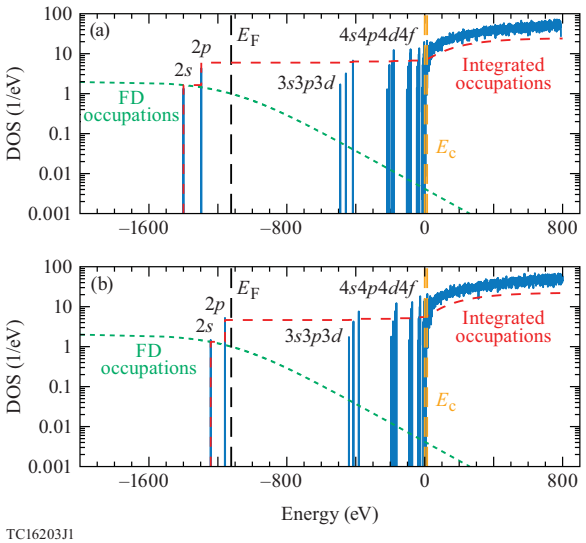

FIG. 1. (a) DOS of Fe at $\rho_{\text{Fe}} = 0.165$ g/cm^3 and $T = 2.11$ MK; (b) DOS of Cr at $\rho_{\text{Cr}} = 0.161$ g/cm^3 and $T = 2.11$ MK. The solid green line shows Fermi-Dirac occupations [Eq. (4)], the solid red line corresponds to the integrated occupation (integrated number of electrons), $N(E)$ defined by Eq. (5), vertical dashed lines indicate locations of the Fermi level, E_F (dashed black) and of the continuum edge, E_F (dashed orange).

$$N(E) = \int_{-\infty}^{E} g(E) f_{\text{FD}}(E) dE, \tag{5}$$

increases with discrete increments for $E < E_c$, changes the slope and starts to behave as $N(E) \propto \text{erf}(E - E_c)$ at $E \geqslant E_c$ approaching the total number of electrons limit at high energy. These calculations were performed for a single atom in a cubic cell, Baldereschi's mean value k point (BMVP) [41], and the ground-state Perdew–Burke–Ernzerhof (PBE) generalized gradient approximation (GGA) exchange-correlation (XC) density functional [42]. See Sec. II B for discussion of finite-size and XC thermal effects. Further computational details are reported in Sec. II C.

B. Equation of state and pair correlation function

Thermodynamic conditions in experiments on Fe and Cr correspond to high reduced temperature [temperature in terms of the Fermi temperature, $T_F = (3\pi^2 n_{\text{free}})^{2/3}/(2k_B)$],

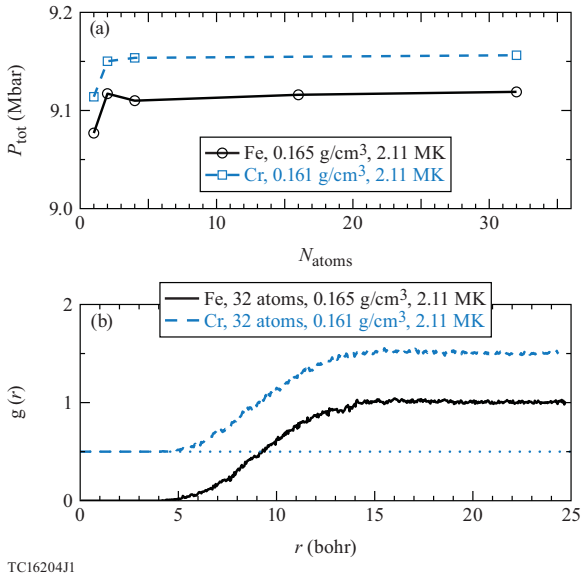

FIG. 2. (a) Convergence of the total pressure with respect to the number of atoms in the OFDFT-MD simulation cell for Fe at $\rho_{Fe} = 0.165$ g/cm^3, and $T = 2.11$ MK and Cr at $\rho_{Cr} = 0.161$ g/cm^3, and $T = 2.11$ MK. (b) The ion pair correlation function from OFDFT-MD simulations for Fe with 32 atoms and for Cr with 32 atoms (shifted by 0.5).

$t = T/T_F \approx 52$ and weak Coulomb coupling, $\Gamma = 2\lambda^2 r_s/t \approx 0.04$, where $\lambda = (4/9\pi)^{1/3}$ and $r_s = [3/(4\pi n_{free})]^{1/3} \approx 3.8$ bohr is the Wigner–Seitz radius. To investigate equation of states and some structural properties such as pair correlation function (PCF) of Fe and Cr under these conditions, we performed AIMD simulations driven by orbital-free DFT forces. Computational details are reported in Sec. II C.

First, we studied the finite-size effects performing AIMD simulations with the number of atoms in the simulation cell ranging between 2 and 32, the Thomas–Fermi (TF) noninteracting free-energy [43], and ground-state local density approximation (LDA) for exchange-correlation [44]. The total pressure as a function of the number of atoms is shown in Fig. 2(a). Pressure variation within 0.1% for both elements indicates negligible finite-size effects. Pressure predicted by the TF average atom model shown in Fig. 2(a) as $N_{atoms} = 1$ data, is also very accurate, underestimating the AIMD value by about only 0.5%. To investigate the importance of the nonhomogeneity and thermal exchange-correlation effects, we additionally performed AIMD simulations employing the ground-state GGA PBE, and finite-temperature Karasiev–Dufty–Trickey (KDT16) GGA [45] exchange correlation functionals. The nonhomogeneity XC effects taken into account at the GGA level by the PBE functional and the combined nonhomogeneity and thermal XC effects taken into account by the thermal GGA KDT16 density functional increase pressure by less than 0.5% within statistical errors. In the latter case, when the ground-state LDA XC is replaced with the thermal KDT16 GGA, the total pressure increases from 9.12 to 9.16 Mbar for Fe and from 9.15 to 9.19 Mbar for Cr. This result is expected. Analysis performed in Ref. [46] for the HEG at finite-temperature suggests that, at given thermodynamic conditions ($t \approx 52$, $r_s \approx 3.8$ bohr), the XC contribution is almost three orders of magnitude smaller compared with the noninteracting or total free energy: At such high temperatures and moderate values of r_s, the XC contribution $\mathcal{F}_{xc}$ to the free energy is negligible compared with the noninteracting free-energy term: $\mathcal{F}_{xc} \ll \mathcal{F}_s$.

Ion pair correlation functions for Fe and Cr as predicted by AIMD simulations with 32 atoms in simulation cell are shown in Fig. 2(b). PCF's at these conditions do not exhibit any structure except a weak correlation peak near 14 bohr. The closest ion–ion approach distance of about 5 bohr is large enough to reduce interaction between neighboring ions and expect small finite-size effects. This is true for pressure calculations [Fig. 2(a)] and for bound–free absorption, but not for the location of bound–bound absorption peaks (see Fig. 4 in the next section).

C. Computational details and convergence tests

We used AIMD simulations driven by the orbital-free (OF) DFT forces. The singularity of the Coulomb electron–ion interaction was regularized via local pseudopotential (LPP) generated at a corresponding thermodynamic condition as described in Ref. [47] by employing the Thomas–Fermi noninteracting free-energy density functional [43] in combination with the ground-state LDA. For consistency, the same combination of the noninteracting free-energy and exchange-correlation density functionals was used in our OF-AIMD simulations performed with the PROFESS@QUANTUMESPRESSO computational package [48]. Employing a more accurate finite-temperature KDT16 GGA exchange-correlation [45] affects results essentially within very small statistical uncertainties (≈0.5% or so, see Sec. II B). The Thomas–Fermi approximation for noninteracting free energy is also very accurate at high temperatures. Two advanced GGA-level noninteracting free-energy density functionals, VT84F [49] and LKTF [50], at high T reduce to the Thomas–Fermi approximation by construction and yield virtually identical results.

In this study we are focused on the L-shell absorption and opacity calculations at temperatures when the deep $1s$ bands remain fully populated. Therefore $1s$ frozen-core projector augmented wave (PAW) data sets for Fe and Cr are generated using the ATOMPAW code [51]. A small augmentation sphere radius $r_{PAW} = 0.35$ bohr requires a relatively high cutoff energy of $E_{cut} = 800$ Ry to converge electronic pressure. The optical properties are calculated using the Kubo–Greenwood formulation implemented within the PAW formalism in KGEC@QUANTUM-ESPRESSO [31,32,48] packages. The Gaussian broadening was done with relatively large $\delta = 15$ eV due to the sparsity of states in the case of the single-atom-in-a-cell calculations.

Tests comparing the ground-state PBE and finite-T KSDT XC functionals provided virtually identical results for the mass absorption coefficients, demonstrating again that the role of the XC functional at these thermodynamic conditions is negligible. Figure 3(a) shows that the mass absorption coefficient (and other optical properties) converges at lower E_{cut}

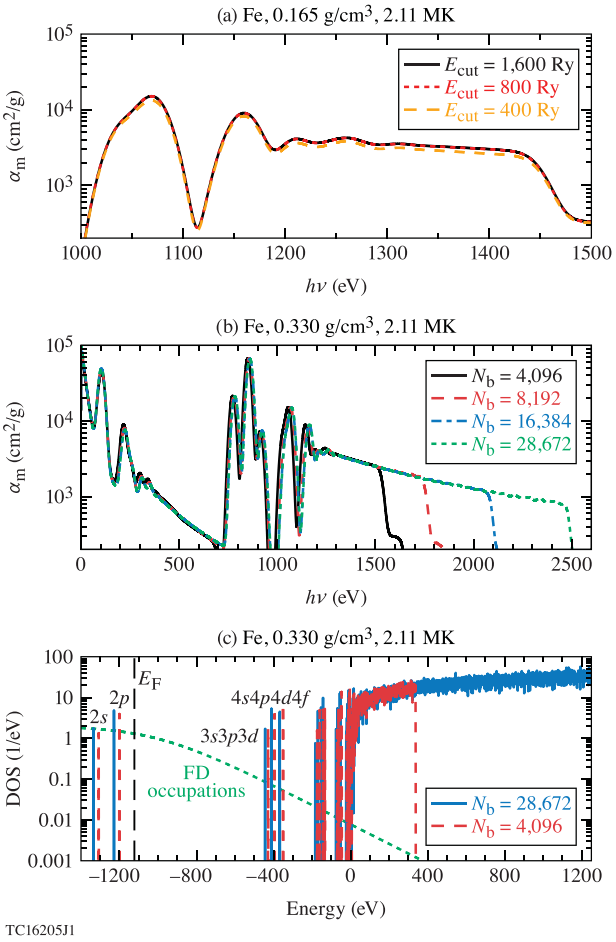

FIG. 3. (a) Convergence of the mass absorption coefficient of Fe with respect to the energy cutoff for a $1s^2$ frozen-core PAW data set with $r_{PAW} = 0.35$ bohr performed for a single-atom-in-a-cell at $\rho_{Fe} = 0.165$ g/cm^3 and $T = 2.11$ MK. Calculations performed with a small number of bands $N_b = 4096$. (b) Convergence of the mass absorption coefficient of Fe with respect to the number of bands included in calculation performed for a single-atom-in-a-cell at $\rho_{Fe} = 0.330$ g/cm^3 and $T = 2.11$ MK. Calculations performed with converged value of $E_{cut} = 800$ Ry. (c) DOS of Fe at $\rho_{Fe} = 0.330$ g/cm^3, and $T = 2.11$ MK calculated for two number of thermally occupied bands, $N_b = 28672$ (solid blue curve) and $N_b = 4096$ (dashed red curve).

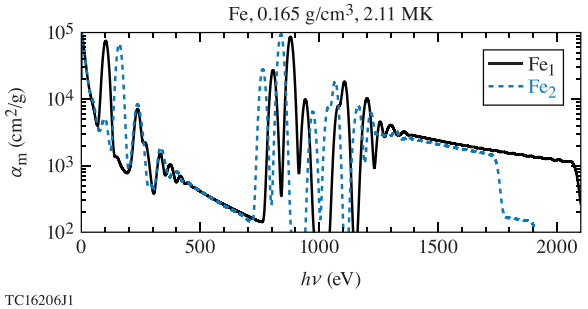

FIG. 4. The mass absorption coefficient of Fe calculated for a single-atom-in-a-cell (Fe_1) and a two-atom MD snapshot (Fe_2) at $\rho_{Fe} = 0.165$ g/cm^3 and $T = 2.11$ MK.

value (as compared with the converged value of E_{cut} for pressure) of 400 Ry.

Convergence of the mass absorption coefficient with respect to the number of thermally occupied bands included in calculation is shown in Fig. 3(b). Calculation with $N_b = 4096$ covers a range of photon energies up to 1500 eV. Increase of N_b between 4096 and 28 672 gradually increases the absorption photon energy range up to 2500 eV. To analyze the importance of free-free contributions and to find out which bound-free transitions contribute into the mass absorption coefficient, we compare the DOS calculated for two values of $N_b = 4096$ and 28 672 shown in Fig. 3(c). Contribution of the L-shell bound-free transitions starts at photon energies around 1200 eV, given by a difference between the continuum edge location ($E_c \approx 0$ eV) and L-shell $2p$ bound level location ($E_{2p} \approx -1200$ eV); for the $N_b = 4096$ calculation, these transitions contribute into the mass absorption coefficient for photon energies up to 1500 eV [shown in Fig. 3(b)]. This value can be estimated as the difference between the highest free-electron state energy ($\approx$350 eV) and E_{2p} bound state location (≈ -1200 eV). The same considerations for the M-shell bound–free transitions lead us to the conclusion that for the $N_b = 4096$ calculation these transitions contribute in the range of photon energies between $\approx$400 eV and $\approx$750 eV, i.e., for calculations with $N_b = 4096$, the M-shell bound–free transitions are not taken into account for the mass absorption in the range of photon energies above 1200 eV. Calculations with $N_b = 28\,672$ account for the M-shell bound-free transitions contribution into the mass absorption in the range of photon energies between $\approx$400 eV and $\approx$1650 eV (estimated as a difference between the highest free-electron state energy ($\approx$1250 eV) and the M-shell bound states location (≈ -400 eV). Taking into account that the mass absorption coefficients for photon energies between 1200 and 1500 eV for calculations with $N_b = 28\,672$ (with the M-shell bound-free transitions taken into account) and with $N_b = 4096$ (the M-shell bound–free transitions are not accounted) are identical, we conclude that the contribution of the M-shell bound-free transitions into the mass absorption coefficient is negligible.

The range of the photon energies for the free-free absorption for calculations with two numbers of bands (4096 and 28 672) included in calculation can be estimated from the DOS exactly on the same way. These two calculations lead to the same value of the absorption coefficient for photon energies up to 1250 eV (when the free–free transitions are taken into account for calculations with $N_b = 28\,672$); thus we conclude that the free-free transitions are also negligible for the L-shell mass absorption (and opacity) calculations.

Lastly, Fig. 4 compares the mass absorption coefficient of Fe calculated for a single atom in a cell, and for a two-atom MD snapshot. A calculation based on the MD snapshot changes the location of bound-bound absorption peaks for photon energies below 1300 eV. The bound-free absorption above 1300 eV is almost identical for the two calculations, except that the single-atom-in-a-cell results cover larger photon energy range because the number of bands per atom included in this calculation is larger compared with the MD snapshot calculation.

At such weakly degenerate and weakly coupled plasma conditions ($t \approx 52$, $\Gamma \approx 0.04$) one may expect that much

TABLE I. Free-electron density (in cm^{-3} units) for chromium and iron at $T = 182$ eV and $\rho_{Cr} = 0.161$ g/cm^3, $\rho_{Fe} = 0.165$, respectively, as predicted by the DFT, REODP, and RSGF methods.

System	DFT	REODP	RSGF
Cr	3.00×10^{22}	2.95×10^{22}	3.12×10^{22}
Fe	3.00×10^{22}	2.95×10^{22}	3.12×10^{22}

simpler approaches, based essentially on semiclassical plasma-screening models [52–54], should be reasonably accurate. However, opacity calculations based on these approaches would represent limiting cases of average-atom models, which are already known not to agree with the Sandia experiments [24,55].

III. RESULTS

In this section we present our results on the free-electron density and the L-shell opacity of chromium and iron as predicted by the DFT, REODP, and RSGF methods and provide a comparison to the pulse-power experimental opacity measurements [14,19].

Table I shows free-electron densities of chromium and iron calculated at $T = 182$ eV and $\rho = 0.161$ g/cm^3 and 0.165 g/cm^3, respectively. Theoretical predictions by all three methods are in very good agreement; relative differences of the REODP and RSGF values with respect to the DFT data do not exceed 2% and 4%, respectively, matching the experimental value of 3×10^{22} cm^{-3} from measurements for Cr and Fe.

Figure 5 shows our main results for opacity of chromium and iron calculated at $T = 182$ eV and material density of 0.161 g/cm^3 and 0.165 g/cm^3, respectively, alongside with experimental measurements. At short wavelengths below ≈9.5Å (the L-shell bound–continuum region for photon energies above ≈1.2 keV), the agreement between all three theoretical data and experiments is very good for chromium. The REODP curve goes straight through the experimental data, while the DFT and RSGF data are located slightly below, touching the shaded gray experimental error bars. The situation for iron is different; opacity predicted by theoretical methods in the L-shell bound-continuum region is underestimated by about 50% as compared with the experimental data. The REODP curve is slightly closer to the experimental data as compared with the DFT single-atom-in-a-cell and RSGF simulations.

In the wavelength range above 9.5 Å opacity is dominated mostly by the bound–bound absorption lines. The DFT and RSGF calculations predict a small set of smooth and strong discrete lines separated by deep windows. The REODP method predicts a richer spectrum of sharp peaks. The REODP-calculated opacities represent the detailed all-line spectra without any kind of averaging into spectral groups. The peaks and wings of lines are resolved with a high accuracy. The spectral lines are roughly centered on the experimental opacity curves. However, none of our theoretical predictions is close to the measured bound-bound opacity in

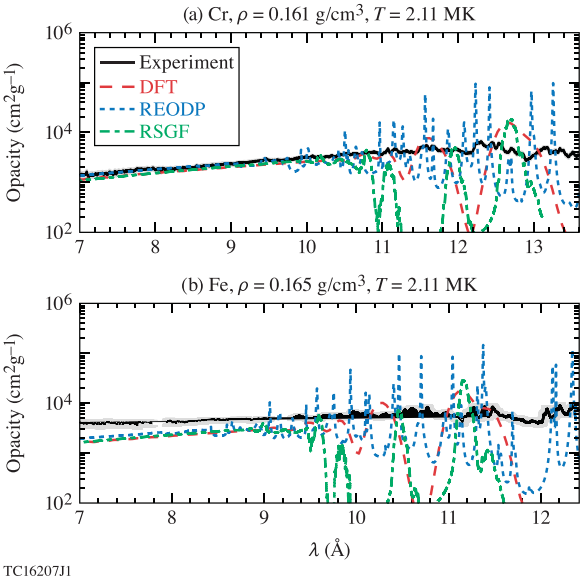

FIG. 5. Opacity of chromium and iron at 0.161 g/cm^3 and 0.165 g/cm^3, respectively. Comparison is made between the experimental measurements (solid black curve, gray shaded area corresponds to the experimental measurements error) and three theoretical predictions done at $T = 182$ eV.

that range. The DFT predictions for the bound-bound absorption can be improved by performing the Kubo–Greenwood optical calculations on top of the AIMD snapshots for larger supercells including more than two atoms, by considering more realistic charge state distributions. However, such demanded calculations, on both memory and time, are currently out of reach.

IV. SUMMARY

Recently proposed DFT-based methodology for optical property predictions of matter in the warm dense regime has been used for calculations of L-shell opacity of iron and chromium with a hope to resolve the previously reported discrepancy between atomic physics code calculations and experimental measurements for Fe in the bound-free range [14,19,29]. First, we estimated the average ionization state and free-electron density from the DFT density of state data and found the iron and chromium material densities corresponding to experimental conditions. Next, the AIMD simulations driven by orbital-free DFT forces were performed to investigate finite-size effects, equation of state and PCF. Eventually, the Kubo–Greenwood optical calculations were performed and the DFT opacity data were compared with the REODP and RSGF models. Good agreement was found between all three theoretical methods in the range of photon energies corresponding to transitions between the L-shell-bound and free-electron states. Theoretical predictions also agree with experimental measurements in that quasicontinuum range for Cr, while the difference between the direct DFT calculations and the experiment for Fe remains close to 50%, very similar to existing calculations from other atomic physics models.

ACKNOWLEDGMENTS

We thank T. Nagayama for providing the experimental data on Cr and Fe. This material is based upon work supported by the Department of Energy National Nuclear Security Administration under Award No. DE-NA0003856, U.S. National Science Foundation PHY Grants No. 1802964 and No. 2205521, Defense Threat Reduction Agency under Grants No. HDTRA1-19-1-0019 and HDTRA1-20-2-0001, the University of Rochester, and the New York State Energy Research and Development Authority. This research used resources of the National Energy Research Scientific Computing Center, a DOE Office of Science User Facility supported by the Office of Science of the U.S. Department of Energy under Contract No. DE-AC02-05CH11231 using NERSC Award No. FES-ERCAP0021234. This report was prepared as an account of work sponsored by an agency of the U.S. Government. Neither the U.S. Government nor any agency thereof, nor any of their employees, makes any warranty, express or implied, or assumes any legal liability or responsibility for the accuracy, completeness, or usefulness of any information, apparatus, product, or process disclosed, or represents that its use would not infringe privately owned rights. Reference herein to any specific commercial product, process, or service by trade name, trademark, manufacturer, or otherwise does not necessarily constitute or imply its endorsement, recommendation, or favoring by the U.S. Government or any agency thereof. The views and opinions of authors expressed herein do not necessarily state or reflect those of the U.S. Government or any agency thereof.

APPENDIX: DETAILS OF KUBO–GREENWOOD OPTICAL CALCULATIONS

Kubo–Greenwood formalism [21,22] is based on the linear response theory and one-electron approximation. In practice, and in our implementation, the one-electron states and corresponding eigenvalues are from a Mermin–Kohn–Sham DFT calculation. Kubo–Greenwood data calculated on a set of statistically independent "snapshots" (a set of fixed ionic configurations) along an AIMD trajectory provide a reliable description of optical properties of matter at wide range of thermodynamic conditions including warm-dense regime. These calculations with KGEC@QUANTUM-ESPRESSO [31,32] include two steps: Solution of Mermin–Kohn–Sham equations and the Kubo–Greenwood postprocessing. Within the MKS formalism, for each lattice configuration snapshot at lattice coordinates $\{\mathbf{R}\}_I$, we obtain N_b thermally occupied states $\psi_{i,\mathbf{k},I}$ and corresponding band energies $\varepsilon_{i,\mathbf{k},I}$ for a given $\mathbf{k}$ point by solving the following system of coupled differential equations:

$$\left\{-\tfrac{1}{2}\nabla^2 + v_\mathrm{ext} + v_\mathrm{H} + v_\mathrm{xc}\right\}\psi_{i,\mathbf{k},I} = \varepsilon_{i,\mathbf{k},I}\psi_{i,\mathbf{k},I}. \tag{A1}$$

Here v_ext is the external (electron-ion) potential, v_H and v_xc are functional derivatives with respect to the electron density of the Hartree energy and the exchange-correlation term respectively. The real and imaginary parts of the KG frequency dependent electrical conductivity are (see details in Ref. [31])

$$\sigma_1(\omega;\{\mathbf{R}\}_I) = \frac{2\pi}{3\omega\Omega}\sum_{\mathbf{k}} \mathrm{w}_\mathbf{k} \sum_{i,j}^{N_b}\sum_{\nu=1}^{3}[f_\mathrm{FD}(\varepsilon_{i,\mathbf{k},I}) - f_\mathrm{FD}(\varepsilon_{j,\mathbf{k},I})]|\langle\psi_{j,\mathbf{k},I}|\nabla_\nu|\psi_{i,\mathbf{k},I}\rangle|^2 \frac{\delta/2}{(\epsilon_{j,\mathbf{k},I} - \epsilon_{i,\mathbf{k},I} - \omega)^2 + \delta^2/4}, \tag{A2}$$

and

$$\sigma_2(\omega;\{\mathbf{R}\}_I) = \frac{2\pi}{3\omega\Omega}\sum_{\mathbf{k}} \mathrm{w}_\mathbf{k} \sum_{i,j}^{N_b}\sum_{\nu=1}^{3}\frac{f_\mathrm{FD}(\varepsilon_{i,\mathbf{k},I}) - f_\mathrm{FD}(\varepsilon_{j,\mathbf{k},I})}{\varepsilon_{i,\mathbf{k},I} - \varepsilon_{j,\mathbf{k},I}}|\langle\psi_{j,\mathbf{k},I}|\nabla_\nu|\psi_{i,\mathbf{k},I}\rangle|^2 \frac{\epsilon_{j,\mathbf{k},I} - \epsilon_{i,\mathbf{k},I} - \omega}{(\epsilon_{j,\mathbf{k},I} - \epsilon_{i,\mathbf{k},I} - \omega)^2 + \delta^2/4}, \tag{A3}$$

where Ω is the system volume, $\mathrm{w}_\mathbf{k}$ is the weight of the Brillouin zone point $\mathbf{k}$, and $f_\mathrm{FD}(\varepsilon_{i,\mathbf{k},I})$ are Fermi-Dirac occupations (4) of MKS bands $\psi_{i,\mathbf{k},I}$. The $\delta/2$ in Eqs. (A2) and (A3) is magnitude of an imaginary factor related to damping or relaxation effects. The Lorentzian in Eq. (A2) can be replaced by a Gaussian with δ width; both functions behave like a Dirac δ function in the limit of the δ width going to zero.

Other properties are calculated directly from the frequency dependent real and imaginary parts of the electrical conductivity. The dielectric function (omitting the ionic configuration dependence)

$$\epsilon(\omega) = \epsilon_1(\omega) + i\epsilon_2(\omega), \tag{A4}$$

where

$$\epsilon_1(\omega) = 1 - \frac{4\pi}{\omega}\sigma_2(\omega), \tag{A5}$$

and

$$\epsilon_2(\omega) = \frac{4\pi}{\omega}\sigma_1(\omega). \tag{A6}$$

The real and imaginary parts of the index of refraction are related to the dielectric function

$$n(\omega) = \sqrt{\frac{1}{2}\{|\epsilon(\omega)| + \epsilon_1(\omega)\}}, \tag{A7}$$

and

$$k(\omega) = \sqrt{\frac{1}{2}\{|\epsilon(\omega)| - \epsilon_1(\omega)\}}. \tag{A8}$$

Eventually the absorption coefficient is calculated as

$$\alpha(\omega) = \sigma_1(\omega)\frac{4\pi}{n(\omega)c}, \tag{A9}$$

where c is the speed of light. Final answers are given by the average of each property of interest over all snapshots.

[1] J. J. Fortney and N. Nettelmann, The interior structure, Composition, and evolution of giant planets, Space Sci. Rev. **152**, 423 (2010).

[2] C. A. Iglesias, F. J. Rogers, and D. Saumon, Density effects on the opacity of cool helium white dwarf, Astrophys. J. Lett. **569**, L111 (2002).

[3] S. X. Hu, L. A. Collins, V. N. Goncharov, T. R. Boehly, R. Epstein R. L. McCrory, and S. Skupsky, First-principles opacity table of warm dense deuterium for inertial-confinement-fusion applications, Phys. Rev. E **90**, 033111 (2014).

[4] S. X. Hu, V. N. Goncharov, T. R. Boehly, R. L. McCrory, S. Skupsky, L. A. Collins, J. D. Kress, and B. Militzer, Impact of first-principles properties of deuteriumtritium on inertial confinement fusion target designs, Phys. Plasmas **22**, 056304 (2015).

[5] J. Colgan, D. P. Kilcrease, N. H. Magee Jr., G. S. J. Armstrong, J. Abdallah Jr., M. E. Sherrill, C. J. Fontes, H. L. Zhang, and P. Hakel, Light element opacities from ATOMIC, High Energy Density Phys. **9**, 369 (2013).

[6] C. A. Iglesias and F. J. Rogers, Opacities for the solar radiative interior, Astrophys. J. **371**, 408 (1991).

[7] Q. Porcherot, J.-C. Pain, F. Gilleron, and T. Blenski, A consistent approach for mixed detailed and statistical calculation of opacities in hot plasmas, High Energy Density Phys. **7**, 234 (2011).

[8] C. Blancard, Ph. Cosse, and G. Faussurier, Solar mixture opacity calculations using detailed configuration and level accounting treatments, Astrophys. J. **745**, 10 (2012).

[9] D. Benredjem, W. Jarrah, F. Gilleron, J.-C. Pain, S. Ferri, and A. Calist, Opacity calculations. Ge and Si dopants in ICF, High Energy Density Phys. **16**, 23 (2015).

[10] V. Dervieux, B. Loupias, S. Baton, L. Lecherbourg, K. Glize, C. Rousseaux, C. Reverdin, L. Gremillet, C. Blancard, V. Silvert, J.-C. Pain, C. R. D. Brown, P. Allan, M. P. Hill, D. J. Hoarty, and P. Renaudin, Characterization of near-LTE, high-temperature and high-density aluminum plasmas produced by ultra-high intensity lasers, High Energy Density Phys. **16**, 12 (2015).

[11] S. J. Rose, Calculations of the radiative opacity of laser-produced plasmas, J. Phys. B: At., Mol. Opt. Phys. **25**, 1667 (1992).

[12] S. J. Rose, New experimental possibilities for measuring radiative opacity under conditions in the sun's interior, Plasma Phys. Control. Fusion **47**, B735 (2005).

[13] D. J. Hoarty, J. Morton, M. Jeffery, L. K. Pattison, A. Wardlow, S. P. D. Mangles, S. J. Rose, C. Iglesias, K. Opachich, R. F. Heeter, and T. S. Perry, A proposal to measure iron opacity at conditions close to the solar convective zone-radiative zone boundary, High Energy Density Phys. **32**, 70 (2019).

[14] J. E. Bailey, T. Nagayama, G. P. Loisel, G. A. Rochau, C. Blancard, J. Colgan, Ph. Cosse, G. Faussurier, C. J. Fontes, F. Gilleron, I. Golovkin, S. B. Hansen, C. A. Iglesias, D. P. Kilcrease, J. J. MacFarlane, R. C. Mancini, S. N. Nahar, C. Orban, J.-C. Pain, A. K. Pradhan *et al.*, A higher-than-predicted measurement of iron opacity at solar interior temperatures, Nature (London) **517**, 56 (2015).

[15] S. X. Hu, L. A. Collins, J. P. Colgan, V. N. Goncharov, and D. P. Kilcrease, Optical properties of highly compressed polystyrene: An *ab initio* study, Phys. Rev. B **96**, 144203 (2017).

[16] S. X. Hu, Continuum Lowering and Fermi-Surface Rising in Strongly Coupled and Degenerate Plasmas, Phys. Rev. Lett. **119**, 065001 (2017).

[17] C. A. Iglesias and P. A. Sterne, Comment on "Continuum Lowering and Fermi-Surface Rising in Strongly Coupled and Degenerate Plasmas," Phys. Rev. Lett. **120**, 119501 (2018).

[18] S. X. Hu, Reply to "Comment on 'Continuum Lowering and Fermi-Surface Rising in Strongly Coupled and Degenerate Plasmas'," Phys. Rev. Lett. **120**, 119502 (2018).

[19] T. Nagayama, J. E. Bailey, G. P. Loisel, G. S. Dunham, G. A. Rochau, C. Blancard, J. Colgan, Ph. Cossé, G. Faussurier, C. J. Fontes, F. Gilleron, S. B. Hansen, C. A. Iglesias, I. E. Golovkin, D. P. Kilcrease, J. J. MacFarlane, R. C. Mancini, R. M. More, C. Orban, J.-C. Pain *et al.*, Systematic Study of *L*-Shell Opacity at Stellar Interior Temperatures, Phys. Rev. Lett. **122**, 235001 (2019).

[20] N. D. Mermin, Thermal properties of the inhomogeneous electron gas, Phys. Rev. **137**, A1441 (1965).

[21] R. Kubo, Statistical-mechanical theory of irreversible processes. I. General theory and simple applications to magnetic and conduction problems, J. Phys. Soc. Jpn. **12**, 570 (1957).

[22] D. A. Greenwood, The Boltzmann equation in the theory of electrical conduction in metals, Proc. Phys. Soc., London **71**, 585 (1958).

[23] V. V. Karasiev and S. X. Hu, Unraveling the intrinsic atomic physics behind x-ray absorption line shifts in warm dense silicon plasmas, Phys. Rev. E **103**, 033202 (2021).

[24] N. M. Gill, C. J. Fontes, and C. E. Starrett, Time-dependent density functional theory applied to average atom opacity, Phys. Rev. E **103**, 043206 (2021).

[25] R. M. More, S. B. Hansen, and T. Nagayama, Opacity from two-photon processes, High Energy Density Phys. **24**, 44 (2017).

[26] M. K. G. Kruse and C. A. Iglesias, Two-photon ionization in solar opacity experiments, High Energy Density Phys. **41**, 100976 (2021).

[27] J. J. Rehr and R. C. Albers, Theoretical approaches to x-ray absorption fine structure, Rev. Mod. Phys. **72**, 621 (2000).

[28] Y. Wang, G. M. Stocks, W. A. Shelton, D. M. C. Nicholson, Z. Szotek, and W. M. Temmerman, Order-*N* Multiple Scattering Approach to Electronic Structure Calculations, Phys. Rev. Lett. **75**, 2867 (1995).

[29] N. R. Shaffer and C. E. Starrett, Dense plasma opacity via the multiple-scattering method, Phys. Rev. E **105**, 015203 (2022).

[30] G. Miloshevsky and A. Hassanein, Atomic and optical properties of warm dense copper, Phys. Rev. E **92**, 033109 (2015).

[31] L. Calderín, V. V. Karasiev, and S. B. Trickey, Kubo-Greenwood electrical conductivity formulation and implementation for projector augmented wave datasets, Comput. Phys. Commun. **221**, 118 (2017).

[32] P. Giannozzi, S. Baroni, N. Bonini, M. Calandra, R. Car, C. Cavazzoni, D. Ceresoli, Guido L. Chiarotti, M. Cococcioni, I. Dabo, A. D. Corso, Stefano de Gironcoli, S. Fabris, G. Fratesi, R. Gebauer, U. Gerstmann, C. Gougoussis, A. Kokalj, M. Lazzeri, L. Martin-Samos *et al.*, QUANTUM ESPRESSO: A modular and open-source software project for quantum simulations of materials, J. Phys.: Condens. Matter **21**, 395502 (2009).

[33] Y. B. Zel'dovich and Y. P. Raizer, *Physics of Shock Waves and High-Temperature Hydrodynamic Phenomena* (Academic, New York, 1966), Vol. I.

[34] M. J. Seaton, Y. Yu, D. Mihalas, and A. K. Pradhan, Opacities for stellar envelopes, Mon. Not. R. Astron. Soc. **266**, 805 (1994).

[35] G. Miloshevsky and A. Hassanein, Emission spectra of Warm Dense Matter plasmas, in *Proceedings of the 2014 IEEE 41st International Conference on Plasma Sciences (ICOPS) held with 2014 IEEE International Conference on High-Power Particle Beams (BEAMS)* (IEEE, Piscataway, NJ, 2014), pp. 1–6, doi: 10.1109/PLASMA.2014.7012456.

[36] J. C. Stewart and K. D. Pyatt, Jr., Lowering of ionization potentials in plasmas, Astrophys. J. **144**, 1203 (1966).

[37] D. Liberman and J. Albritton, Dense plasma equation of state model, J. Quant. Spectrosc. Radiat. Transfer **51**, 197 (1994).

[38] C. E. Starrett, N. M. Gill, T. Sjostrom, and C. W. Greeff, Wide ranging equation of state with Tartarus: A hybrid Green's function/orbital based average atom code, Comput. Phys. Commun. **235**, 50 (2019).

[39] W. R. Johnson, C. Guet, and G. F. Bertsch, Optical properties of plasmas based on an average-atom model, J. Quant. Spectrosc. Radiat. Transfer **99**, 327 (2006).

[40] A. Shvydky, A. V. Maximov, V. V. Karasiev, D. Haberberger, S. X. Hu, and V. N. Goncharov, Ionization state and dielectric constant in cold rarefied hydrocarbon plasmas of inertial confinement fusion, Phys. Rev. E **104**, 045207 (2021).

[41] A. Baldereschi, Mean-value point in the Brillouin zone, Phys. Rev. B **7**, 5212 (1973).

[42] J. P. Perdew, K. Burke, and M. Ernzerhof, Generalized Gradient Approximation Made Simple, Phys. Rev. Lett. **77**, 3865 (1996); **78**, 1396(E) (1997).

[43] R. P. Feynman, N. Metropolis, and E. Teller, Equation of state of elements based on the generalized Fermi-Thomas theory, Phys. Rev. **75**, 1561 (1949).

[44] J. P. Perdew and A. Zunger, Self-interaction correction to density-functional approximations for many-electron systems, Phys. Rev. B **23**, 5048 (1981).

[45] V. V. Karasiev, J. Dufty, and S. B. Trickey, Non-Empirical Semi-local Free-Energy Density Functional for Matter Under Extreme Conditions, Phys. Rev. Lett. **120**, 076401 (2018).

[46] V. V. Karasiev, S. B. Trickey, and J. W. Dufty, Status of free-energy representations for the homogeneous electron gas, Phys. Rev. B **99**, 195134 (2019).

[47] F. Lambert, J. Clérouin, and G. Zérah, Very-high-temperature molecular dynamics, Phys. Rev. E **73**, 016403 (2006).

[48] V. V. Karasiev, T. Sjostrom, and S. B. Trickey, Finite-temperature orbital-free DFT molecular dynamics: Coupling PROFESS and QUANTUM ESPRESSO, Comput. Phys. Commun. **185**, 3240 (2014).

[49] V. V. Karasiev, D. Chakraborty, O. A. Shukruto, and S. B. Trickey, Nonempirical generalized gradient approximation free-energy functional for orbital-free simulations, Phys. Rev. B **88**, 161108(R) (2013).

[50] K. Luo, V. V. Karasiev, and S. B. Trickey, Towards accurate orbital-free simulations: A generalized gradient approximation for the noninteracting free energy density functional, Phys. Rev. B **101**, 075116 (2020).

[51] N. A. W. Holzwarth, A. R. Tackett, and G. E. Matthews, A projector augmented wave (PAW) code for electronic structure calculations, Part I: *Atompaw* for generating atom-centered functions, Comput. Phys. Commun. **135**, 329 (2001).

[52] C. Deutsch, Nodal expansion in a real matter plasma, Phys. Lett. A **60**, 317 (1977).

[53] C. Deutsch, M. M. Gombet, and H. Minoo, Classical modelization of symmetry effects in the dense high-temperature electron gas, Phys. Lett. A **66**, 381 (1978).

[54] C. Deutsch and M. M. Gombert, Diffraction corrections to the equilibrium properties of the classical electron gas. Pair correlation function, J. Math. Phys. **17**, 1077 (1976).

[55] M. Krief, Y. Kurzweil, A. Feigel, and D. Gazit, The effect of ionic correlations on radiative properties in the solar interior and terrestrial experiments, Astrophys. J. Lett. **856**, 135 (2018).